The Astrophysical Journal Letters, 843:L9 (6pp), 2017 July 1 https://doi.org/10.3847/2041-8213/aa79f0

Critical Height of the Torus Instability in Two-ribbon Solar Flares

Dong Wang[1,2], Rui Liu[1], Yuming Wang[1], Kai Liu [1], Jun Chen[1], Jiajia Liu[1], Zhenjun Zhou[1], and Min Zhang[2]
[1] CAS Key Laboratory of Geospace Environment, Department of Geophysics and Planetary Sciences, University of Science and Technology of China, Hefei, Anhui 230026, China; rliu@ustc.edu.cn
[2] Department of Mathematics and Physics, Anhui Jianzhu University, Hefei 230601, China
Received 2017 April 14; revised 2017 June 9; accepted 2017 June 9; published 2017 June 27

Abstract

We studied the background field for 60 two-ribbon flares of M-and-above classes during 2011–2015. These flares are categorized into two groups, i.e., *eruptive* and *confined* flares, based on whether a flare is associated with a coronal mass ejection or not. The background field of source active regions is approximated by a potential field extrapolated from the B_z component of vector magnetograms provided by the Helioseismic and Magnetic Imager. We calculated the decay index n of the background field above the flaring polarity inversion line, and defined a critical height $h_{\rm crit}$ corresponding to the theoretical threshold ($n_{\rm crit} = 1.5$) of the torus instability. We found that $h_{\rm crit}$ is approximately half of the distance between the centroids of opposite polarities in active regions and that the distribution of $h_{\rm crit}$ is bimodal: it is significantly higher for confined flares than for eruptive ones. The decay index increases monotonously with increasing height for 86% (84%) of the eruptive (confined) flares but displays a saddle-like profile for the rest, 14% (16%), which are found exclusively in active regions of multipolar field configuration. Moreover, n at the saddle bottom is significantly smaller in confined flares than that in eruptive ones. These results highlight the critical role of background field in regulating the eruptive behavior of two-ribbon flares.

Key words: instabilities – Sun: coronal mass ejections (CMEs) – Sun: flares – Sun: magnetic fields

1. Introduction

Solar flares and coronal mass ejections (CMEs) are among the most energetic phenomena in the solar system. They are often associated with each other and hence believed to be governed by the same physical process (Zhang et al. 2001, 2004; Priest & Forbes 2002; Harrison 2003). In the "standard" picture (Shibata 1998), a positive feedback is established between the slow rising of a magnetic flux rope and magnetic reconnection underneath; as a result, the flux rope erupts into interplanetary space as a CME, and the reconnection is mapped to the solar surface as two-flare ribbons. However, some flares may exhibit circular-shaped (e.g., Liu et al. 2015) or X-shaped ribbons (e.g., Liu et al. 2016b), and not all flares are associated with CMEs (Yashiro et al. 2005). Conventionally, flares are categorized as eruptive flares (with CME association) and confined flares (without CME association). Wang & Zhang (2007) suggested that eruptive flares differ from confined ones in both the energy release location and the ratio between magnetic flux in the low ($<1.1\ R_\odot$) and high ($>1.1\ R_\odot$) corona. Relevant to the ratio is the torus instability, which has been recognized as a pertinent MHD instability underlying solar eruptions from both theoretical (van Tend & Kuperus 1978; Kliem & Török 2006; Aulanier et al. 2010) and observational perspectives (e.g., Török & Kliem 2005; Liu 2008; Cheng et al. 2011; Xu et al. 2012; Zuccarello et al. 2014; Sun et al. 2015; Liu et al. 2016). The torus instability occurs when the external field above the flux rope decreases too rapidly with increasing height, which is quantified by the decay index $n = -d\ln B/d\ln h$. The threshold value of the instability $n_{\rm crit}$ is derived to be 1.5 for a toroidal current channel (Kliem & Török 2006), while for a very flat, nearly two-dimensional current channel, $n_{\rm crit} \gtrsim 1$ (Démoulin & Aulanier 2010). On the other hand, some numerical studies (e.g., Fan & Gibson 2007; Kliem et al. 2013; Zuccarello et al. 2016) and laboratory experiments (Myers et al. 2015, 2016, 2017) found that $n_{\rm crit}$ is in the range [1.4–2.0].

Before the above discrepancy is resolved, we simply take $n_{\rm crit} = 1.5$ as a yardstick number and define the height corresponding to $n_{\rm crit}$ as *critical height* $h_{\rm crit}$ to quantify the onset point of the torus instability. We carried out a comprehensive investigation to evaluate to what extent the decay index affects solar eruptions, which has significant implications for space weather forecasting. We selected events from two-ribbon flares occurring during 2011–2015. The working assumption is that a magnetic flux rope is present in a classical two-ribbon flare, no matter if the rope pre-exists (e.g., Liu et al. 2010) or is newly formed (e.g., Wang et al. 2017). In the sections that follow, we elaborate on the procedure of calculation in Section 2 and give the statistical results and concluding remarks in Section 3.

2. Observation and Analysis

2.1. Instruments

This study mainly used data from the Helioseismic and Magnetic Imager (HMI; Scherrer et al. 2012) and the Atmospheric Imaging Assembly (AIA; Lemen et al. 2011) on board the *Solar Dynamics Observatory* (Pesnell et al. 2012), which was launched on 2010 February 11. HMI's `hmi.sharp_cea` data series provide disambiguated vector magnetograms that are deprojected to the heliographic coordinates with a Lambert (cylindrical equal area, CEA) projection method, at a cadence of 720 s and a pixel scale of $0\overset{\circ}{.}03$ (or 0.36 Mm; Bobra et al. 2014). Flares are monitored by the *Geostationary Operational Environmental Satellite* in soft X-ray (SXR) irradiance and by AIA's seven EUV imaging passbands (94, 131, 171, 193, 211, 304, and 335 Å) and two UV imaging passbands (1600 and 1700 Å) with a spatial resolution of $1\overset{''}{.}5$ and a temporal cadence of 12 s (24 s) for EUV (UV) passbands (Lemen et al. 2011). To obtain the context of CMEs, we examined coronagraph images obtained

by *Solar and Heliospheric Observatory* (*SOHO*) and *Solar Terrestrial Relations Observatory* (*STEREO*).

2.2. Selection and Category of Events

Sixty two-ribbon flares of M- and X-class are selected in this study (Table 1) according to observations of UV flare ribbons in the chromosphere and of EUV post-flare arcades in the corona. The selection criterion is that the center of the source active region is located within ∼45° from the solar disk center, so that the measurements of the photospheric magnetic field are relatively reliable. Flares are categorized as either "E" (eruptive) or "C" (confined) in Table 1. To determine whether a flare is associated with a CME, we collated coronagraph images obtained by *SOHO* and *STEREO*, and EUV images obtained by AIA. The *SOHO* LASCO CME catalog[3] provides a benchmark reference for this purpose. Taking into account the timing and location of flares relative to CMEs as well as the CME speed and direction, we identified 35 eruptive and 25 confined flares (Table 1).

2.3. Decay Index and Critical Height

According to an analytical model of torus instability, a toroidal flux ring is unstable to lateral expansion if the external poloidal field $B_{\rm ex}$ decreases rapidly with increasing height such that the decay index $n = -d\ln B_{\rm ex}/d\ln h$ exceeds $3/2$ (Kliem & Török 2006). Due to the difficulty in decoupling $B_{\rm ex}$ from the flux-rope field in either simulation or observation, a conventional practice is to approximate $B_{\rm ex}$ with a current-free potential field (e.g., Fan & Gibson 2007; Török & Kliem 2007; Liu 2008; Démoulin & Aulanier 2010). In our study, the coronal potential field is extrapolated from the B_z component of the vector magnetograms for active regions, using a Fourier transformation method (Alissandrakis 1981).

Hence, in our calculation, $n = -d\ln B_t/d\ln h$, where B_t denotes the transverse component of the extrapolated potential field, i.e., $B_t = \sqrt{B_x^2 + B_y^2}$. Precisely speaking, it is the external field component orthogonal to the axial current of the flux rope that creates the downward $\boldsymbol{J}\times\boldsymbol{B}$ force. B_t often serves as a good approximation since potential field is almost orthogonal to PIL, along which a flux rope in equilibrium typically resides. One needs keep in mind that this approximation works better with less curved PILs. Here, we take as an example the confined flare on 2014 October 22 in NOAA AR 12192 (No. 52 in Table 1; see also Sun et al. 2015; Liu et al. 2016a) to demonstrate how the critical height $h_{\rm crit}$ is calculated. Figure 1(a) shows a pre-flare photospheric B_z map of AR 12192 at 13:48 UT prior to the onset of the flare, and Figure 1(b) shows the flare ribbons observed near the SXR peak at 14:28 UT in AIA 1600 Å. We sampled the segment of polarity inversion line (PIL) that is located in between the two-flare ribbons (referred to as "flaring PIL" hereafter) by clicking on it as uniformly as possible to get sufficient representative points (marked by crosses), and then calculated decay index n at different heights at these selected points. In Figure 1(c), we plot n as a function of h, which is averaged over the selected points, with the error bar indicating the standard deviation. We located the critical height corresponding to $n = 1.5$ by linear interpolation between the discrete $n(h)$ points, which have a step of 0.36 Mm, and similarly we located the height at $n = 1.5$ on the $n + \delta n$ and $n - \delta n$ profile, where δn is the standard deviation at each $n(h)$ point, to get an uncertainty estimation of critical height. For this case, we obtained that $h_{\rm crit} = 70.6^{+8.4}_{-7.9}$ Mm. As a comparison, Figures 1(d)–(f) show an eruptive flare taking place on 2012 March 14 (No. 12). The corresponding $h_{\rm crit} = 31.1^{+7.8}_{-9.6}$ Mm is much smaller than the confined case.

To evaluate the complexity of magnetic field in active regions and its impact on $h_{\rm crit}$, we calculated the centroids of positive and negative magnetic fluxes for each active region and their distance d. We propose that the magnetic field relevant to a flare of interest can be deemed the dipolar field (labeled "D" in Table 1) if the centroids of opposite polarities are located at two sides of, and their connection passes through, the flaring PIL (e.g., Figure 1(a)). In contrast, the magnetic field is deemed the multipolar field (labeled "M" in Table 1) if the connection of centroids fails to pass through (e.g., Figure 1(d)), or is almost parallel to, the flaring PIL. The latter category includes some cases in which the active region of interest cannot be clearly separated from a neighboring active region (labeled "M*" in Table 1). By visual inspection, we confirmed that this categorization gives a result consistent with the conventional view of dipolar and multipolar fields.

3. Results

The distribution of $h_{\rm crit}$ for the sample of 60 two-ribbon flares is shown in the top panel of Figure 2. The total distribution of $h_{\rm crit}$ peaks at the heights of 20–30 Mm, but for confined flares $h_{\rm crit}$ significantly spreads to higher heights than eruptive flares. The average $h_{\rm crit}$ is 36.3 ± 17.4 Mm for the 35 eruptive flares, and 53.6 ± 21.3 Mm for the 25 confined flares. $h_{\rm crit}$ is highly correlated with the centroid distance d of active regions (bottom panel of Figure 2). From the linear fittings using a least absolute deviation method (`LADFIT` in IDL), we obtained an empirical formula

$$h_{\rm crit} \simeq \frac{1}{2}d, \tag{1}$$

which may serve as a rule of thumb for the scale of $h_{\rm crit}$. In comparison to numerical models, Kliem et al. (2014, Equation (15)) found that within the framework of the active-region model developed by Titov & Démoulin (1999), $h_{\rm crit}/L$ is slightly below unity, where L is the half distance between two monopoles. This is derived for a freely expanding torus without being line-tied. In the numerical experiments with a line-tying surface (Török & Kliem 2007, their Figures 2 and 3), one can also see that for bipolar configurations $h_{\rm crit}$ increases when the distance between external sources increases and that Equation (1) approximately holds for each case (T. Török 2017, private communication). On the other hand, $h_{\rm crit}$ is found to be comparable to the horizontal distance between two sub-photospheric monopoles in a series of numerical simulations imposing different photospheric flows and diffusive coefficients (Aulanier et al. 2010; Zuccarello et al. 2015, 2016). Generally speaking, $h_{\rm crit}$ may be affected by various factors including, but not limited to, (1) functional form of the external field; (2) other external sources besides the dipole confining the flux rope; and (3) depths of the external sources below the surface. For example, in Török & Kliem (2007), the monopoles

[3] http://cdaw.gsfc.nasa.gov/CME_list/index.html

Table 1
Flare List

Number	Date	Time[a]	Location		Class	Category[c]	Profile[d]	Configuration[e]	h_{crit}
	YYYY MM DD	hh mm	AR	Position[b]					(Mm)
1	2011 Mar 07	1430	11166	N11E21	M1.7	E	I	D	$46.8^{+3.2}_{-3.2}$
2	2011 Aug 02	0619	11261	N17W22	M1.4	E	I	M	$22.2^{+5.1}_{-6.0}$
3	2011 Oct 01	0959	11305	N10W06	M1.2	E	I	M	$24.1^{+2.5}_{-1.9}$
4	2011 Oct 02	0050	11305	N09W12	M3.9	E	I	M	$19.4^{+2.8}_{-2.3}$
5	2011 Dec 26	0227	11387	S21W33	M1.5	E	S	M	$11.6^{+3.9}_{-1.6}$
6	2011 Dec 26	2030	11387	S21W44	M2.3	E	S	M	$9.3^{+3.6}_{-1.9}$
7	2012 Jan 19	1605	11402	N32E27	M3.2	E	I	M*	$46.9^{+6.0}_{-5.0}$
8	2012 Jan 23	0359	11402	N28W21	M8.7	E	I	M*	$46.0^{+5.9}_{-6.1}$
9	2012 Mar 07	0024	11429	N18E31	X5.4	E	I	D	$38.6^{+2.9}_{-3.4}$
10	2012 Mar 07	0114	11429	N15E26	X1.3	E	I	D	$39.1^{+7.5}_{-8.1}$
11	2012 Mar 10	1744	11429	N17W24	M8.4	E	I	D	$62.4^{+10.4}_{-19.9}$
12	2012 Mar 14	1521	11432	N13E05	M2.8	E	I	M	$31.1^{+7.8}_{-9.6}$
13	2012 Mar 15	0752	11432	N14W03	M1.8	E	I	M	$40.7^{+2.4}_{-3.0}$
14	2012 Jun 06	2006	11494	S19W05	M2.1	E	I	M*	$20.0^{+1.4}_{-1.4}$
15	2012 Jun 14	1435	11504	S19E06	M1.9	E	I	D	$45.8^{+4.4}_{-4.7}$
16	2012 Jul 05	1318	11515	S16W43	M1.2	E	I	M*	$68.9^{+5.6}_{-5.2}$
17	2012 Jul 12	1649	11520	S13W03	X1.4	E	I	M*	$36.0^{+5.0}_{-5.3}$
18	2013 May 16	2153	11748	N11E40	M1.3	E	I	M*	$21.9^{+2.4}_{-2.4}$
19	2013 Aug 12	1041	11817	S21E18	M1.5	E	I	M*	$22.9^{+3.4}_{-2.7}$
20	2013 Oct 13	0043	11865	S22E17	M1.7	E	S	M	$15.3^{+7.5}_{-4.3}$
21	2013 Oct 28	1153	11877	S16W44	M1.4	E	I	D	$69.7^{+3.4}_{-3.0}$
22	2014 Feb 12	0425	11974	S12W02	M3.7	E	S	M	$64.8^{+10.6}_{-14.0}$
23	2014 Dec 17	0110	12242	S20E08	M1.5	E	I	M*	$26.6^{+4.3}_{-3.9}$
24	2014 Dec 17	0150	12241	S11E33	M1.1	E	I	M	$15.9^{+11.4}_{-3.6}$
25	2014 Dec 17	0451	12242	S18E08	M8.7	E	I	M*	$27.7^{+5.7}_{-5.1}$
26	2014 Dec 20	0028	12242	S19W29	X1.8	E	I	M	$40.5^{+4.3}_{-4.5}$
27	2014 Dec 21	1217	12241	S13W25	M1.0	E	I	M	$51.7^{+8.2}_{-21.5}$
28	2015 Mar 09	2353	12297	S18E45	M5.8	E	I	M	$31.9^{+5.8}_{-6.2}$
29	2015 Mar 15	2322	12297	S19W32	M1.2	E	I	M	$20.1^{+5.6}_{-5.3}$
30	2015 Mar 16	1058	12297	S17W38	M1.6	E	S	M	$16.8^{+1.9}_{-2.5}$
31	2015 Jun 21	0142	12371	N12E13	M2.0	E	I	D	$46.3^{+10.3}_{-12.9}$
32	2015 Jun 22	1823	12371	N13W06	M6.5	E	I	D	$31.6^{+12.3}_{-8.5}$
33	2015 Jun 25	0816	12371	N12W40	M7.9	E	I	D	$56.6^{+5.7}_{-7.4}$
34	2015 Nov 04	1352	12443	N08W02	M3.7	E	I	D	$68.7^{+3.9}_{-4.4}$
35	2015 Nov 09	1312	12449	S13E39	M3.9	E	I	M*	$35.3^{+3.3}_{-4.5}$
36	2011 Mar 09	1107	11166	N09W06	M1.7	C	I	D	$46.9^{+7.1}_{-8.5}$
37	2011 Aug 03	0432	11261	N17E12	M1.7	C	S	M	$16.9^{+2.0}_{-1.6}$
38	2011 Nov 05	0335	11339	N20E45	M3.7	C	I	M	$74.5^{+8.2}_{-7.6}$
39	2011 Nov 05	1121	11339	N19E41	M1.1	C	I	M	$74.9^{+8.9}_{-8.3}$
40	2011 Nov 06	0103	11339	N21E33	M1.2	C	I	M	$82.2^{+9.7}_{-9.3}$
41	2011 Dec 31	1315	11389	S25E46	M2.4	C	I	M*	$61.4^{+1.9}_{-2.3}$
42	2011 Dec 31	1626	11389	S26E42	M1.5	C	I	M*	$62.5^{+2.5}_{-3.4}$
43	2012 Mar 06	1241	11429	N18E36	M2.1	C	I	D	$37.9^{+5.1}_{-7.6}$
44	2012 Apr 27	0824	11466	N11W30	M1.0	C	I	M*	$27.2^{+2.1}_{-2.0}$
45	2012 May 09	1408	11476	N06E22	M1.8	C	I	M	$33.6^{+4.1}_{-3.8}$
46	2012 Jul 10	0514	11520	S16E35	M1.7	C	I	M*	$38.4^{+3.6}_{-4.2}$
47	2013 Nov 01	1953	11884	S12E01	M6.3	C	S	M*	$71.2^{+6.7}_{-7.2}$
48	2014 Feb 04	0400	11967	S14W07	M5.2	C	S	M	$28.4^{+7.5}_{-6.6}$
49	2014 Feb 06	2305	11967	S15W48	M1.5	C	S	M	$19.4^{+5.4}_{-3.3}$
50	2014 Oct 20	0911	12192	S16E42	M3.9	C	I	D	$78.7^{+11.8}_{-14.1}$
51	2014 Oct 20	1637	12192	S14E39	M4.5	C	I	D	$82.1^{+12.6}_{-15.2}$
52	2014 Oct 22	1428	12192	S14E13	X1.6	C	I	D	$70.6^{+8.4}_{-7.9}$
53	2014 Oct 24	2141	12192	S22W21	X3.1	C	I	D	$84.0^{+10.5}_{-9.9}$
54	2014 Dec 01	0641	12222	S22E17	M1.8	C	I	M*	$57.1^{+1.6}_{-1.4}$
55	2014 Dec 17	1901	12241	S10E23	M1.4	C	I	M	$48.6^{+6.6}_{-6.1}$
56	2014 Dec 18	2158	12241	S11E10	M6.9	C	I	M	$54.7^{+5.6}_{-4.9}$
57	2014 Dec 19	0944	12242	S19W27	M1.3	C	I	M*	$48.7^{+17.1}_{-9.5}$

Table 1
(Continued)

Number	Date YYYY MM DD	Time[a] hh mm	Location AR	Location Position[b]	Class	Category[c]	Profile[d]	Configuration[e]	h_{crit} (Mm)
58	2015 Jan 03	0947	12253	S05E16	M1.1	C	I	D	$58.9^{+1.9}_{-2.5}$
59	2015 Jan 04	1536	12253	S05E01	M1.3	C	I	D	$62.5^{+0.8}_{-0.8}$
60	2015 Mar 11	1851	12297	S15E18	M1.0	C	I	M	$19.6^{+5.2}_{-6.4}$

Notes.
[a] GOES 1–8 Å peak time.
[b] Flare position provided by GOES.
[c] "E" for eruptive flares, "C" for confined flares.
[d] "I" for monotonous increasing of n as a function of h, "S" for a saddle-like $n(h)$ profile.
[e] "D" for a dipolar magnetic field, "M" for a multipolar field, and "M*" indicates that the active region of interest is too close to be separated from a neighboring active region.

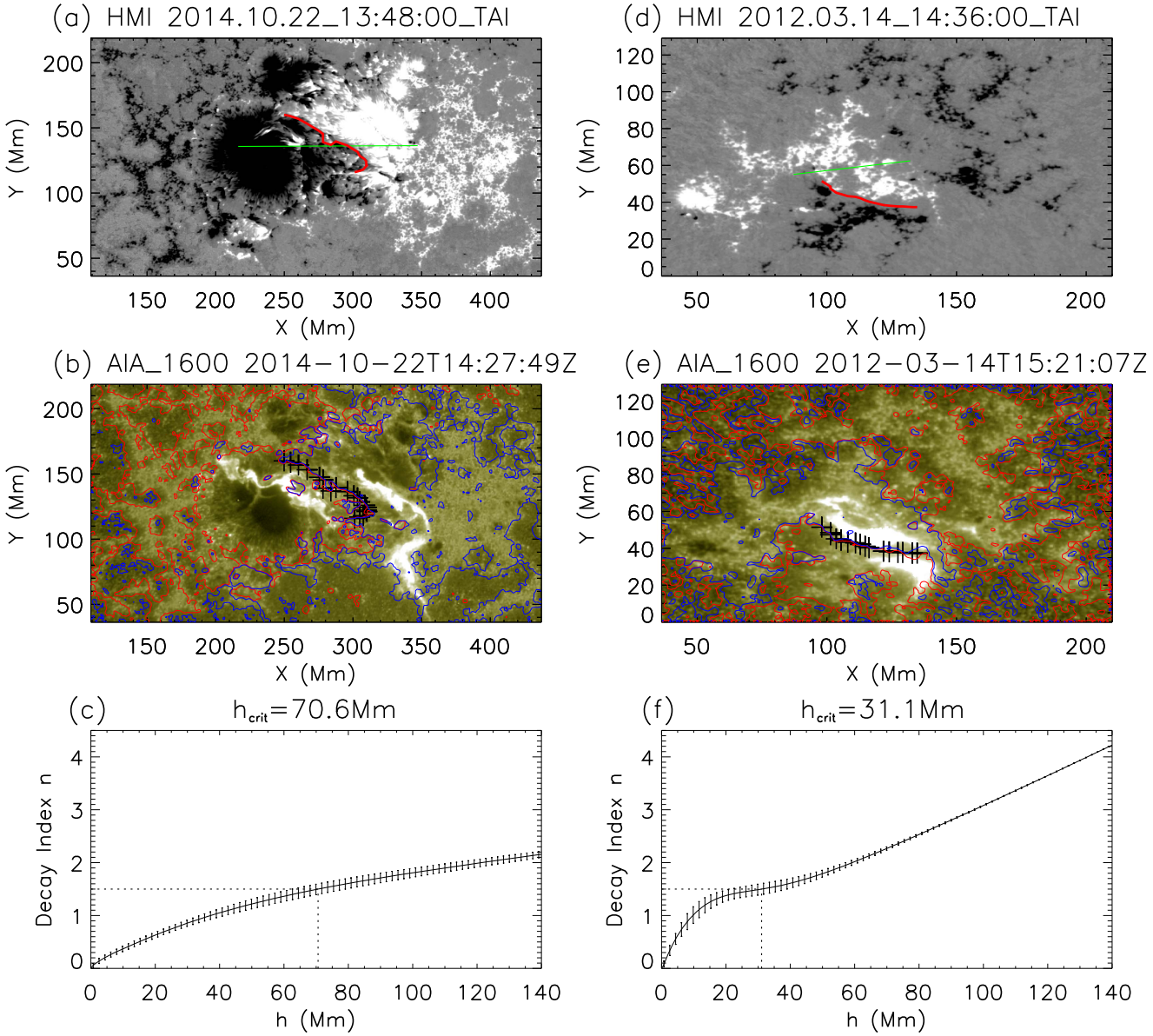

Figure 1. Derivation of the decay index profile for two exemplary events, a confined flare (No. 52) on the left and an eruptive flare (No. 12) on the right. ((a) and (d)) HMI B_z map. The red line denotes the flaring PIL and the green line connects the centroids of opposite polarities. ((b) and (e)) The AIA 1600 Å image overlaid by the B_z contour (50 and 10 G), with red (blue) colors indicating negative (positive) polarity. The sign "+" denotes the points selected along the flaring PIL. ((c) and (f)) The decay index n as a function of the height h above the surface in units of Mm. Dotted lines indicate where n_{crit} and h_{crit} are taken.

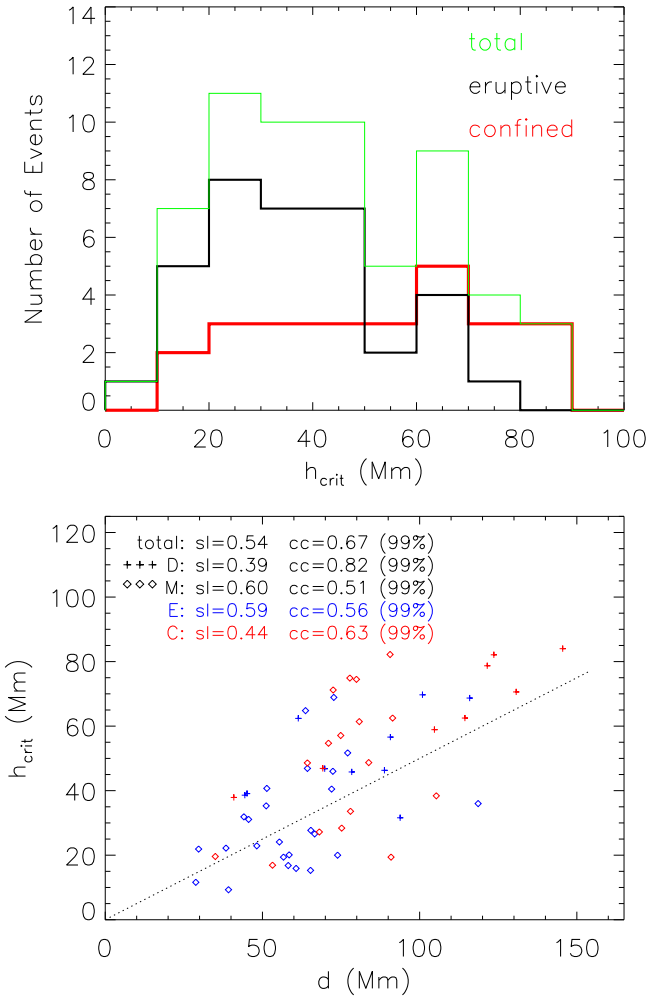

Figure 2. Distribution of $h_{\rm crit}$ (top) and its relation to the centroid distance d of active regions (bottom). In the bottom panel, the plus and diamond symbols denote dipolar (D) and multipolar (M) magnetic field, respectively. Eruptive (E) and confined (C) events are shown in blue and red, respectively. "sl" indicates the slope given by linear fitting and "cc" the correlation coefficient with the confidence interval denoted in the brackets. $h_{\rm crit} = \frac{1}{2}d$ is marked by the dotted line.

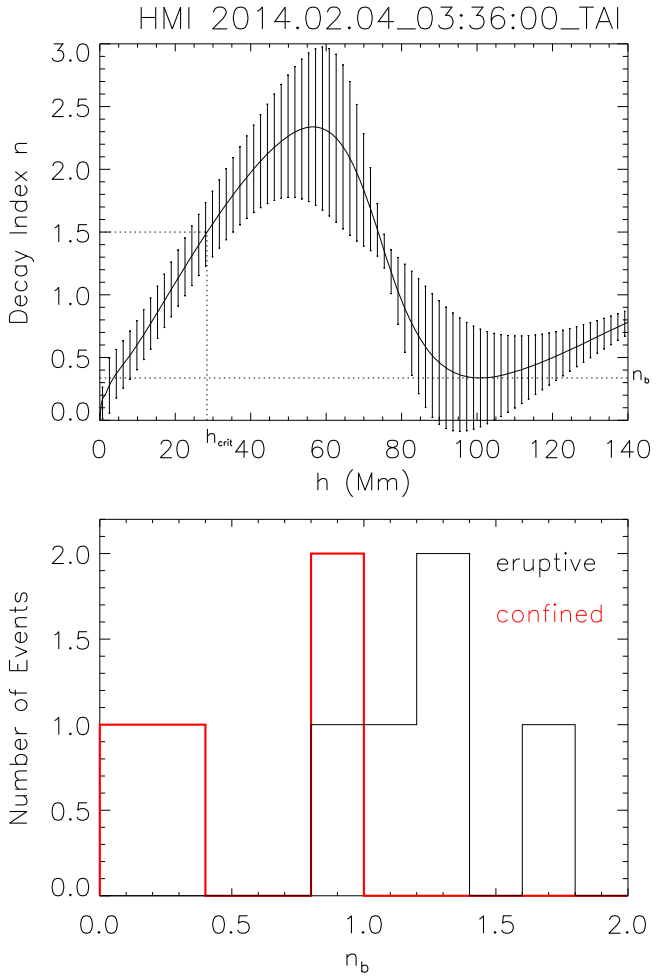

Figure 3. Saddle-like $n(h)$ profile. Top panel shows an exemplary $n(h)$ profile from the confined flare on 2014 February 4 (No. 48 in Table 1). n_b and $h_{\rm crit}$ are marked. Bottom panel shows the distribution of n_b for five eruptive (black) and four confined (red) flares.

are very close to the surface, as compared to the significant depths set in Aulanier et al. (2010).

Two distinct types of $n(h)$ profiles emerge in this investigation, similar to a much smaller sample of nine flares studied by Cheng et al. (2011): (1) n increases monotonically as the height increases in 30 of 35 (86%) eruptive flares and in 21 of 25 (84%) confined flares; and (2) the rest of the $n(h)$ profiles are saddle-like, exhibiting a local minimum at a height higher than $h_{\rm crit}$ (e.g., top panel of Figure 3). The saddle-like profile provides a potential to confine an eruptive structure if the local minimum n_b at the bottom of the saddle is significantly below $n_{\rm crit}$ and the eruption has not developed a large enough disturbance when the eruptive structure reaches the height of n_b. For example, the deep saddle bottom at higher altitudes than $h_{\rm crit}$ may help confine the eruption on 2014 February 4 (top panel of Figure 3). For the nine flares exhibiting a saddle-like $n(h)$ profile, including five eruptive and four confined flares, the distribution of n_b is given in the bottom panel Figure 3. One can see that n_b of the five eruptive flares (black) is generally larger than that of the four confined flares (red). In relation to the field configuration, an outstanding characteristic for saddle-like profiles is that all nine

Table 2
Flare Statistics

	E	C	I	S
D	10	8	18	0
M (M*)	25(10)	17(7)	33(16)	9(1)

Note. Number of different types of flares (E and C) and of $n(h)$ profiles (I and S) in relation to magnetic field configuration (D and M) of active regions. The same notations are adopted here as in Table 1.

events originate from the multipolar magnetic field (Table 2). However, it is not clear exactly what kind of photospheric flux distribution would yield the saddle shape because, on the one hand, the relevant magnetic field is highly complex; on the other hand, the majority cases of monotonously growing $n(h)$ also originates from the multipolar field (Table 2). This will be considered in a future investigation.

To conclude, this investigation confirms that the decay index profile of the background field plays an important role in deciding whether a two-ribbon flare would lead up to a CME. Moreover, the saddle-like profile present in some active regions may provide an additional confinement effect on eruptions.

These results indicate the possibility that some two-ribbon flares might be innately incapable of producing CMEs.

The authors thank the anonymous reviewer for constructive comments that helped greatly improve this Letter. D.W. acknowledges the support by Natural Science Foundation of Anhui province education department (KJ2016JD18, KJ2017A493). R.L. acknowledges the support by NSFC 41474151 and the Thousand Young Talents Program of China, and thanks T. Török for helpful comments. Y.W. acknowledges the support from NSFC 41131065 and 41574165. This work was also supported by NSFC 41421063, CAS Key Research Program KZZD-EW-01-4, and the fundamental research funds for the central universities.

References

Alissandrakis, C. E. 1981, A&A, 100, 197
Aulanier, G., Török, T., Démoulin, P., & DeLuca, E. E. 2010, ApJ, 708, 314
Bobra, M. G., Sun, X., Hoeksema, J. T., et al. 2014, SoPh, 289, 3549
Cheng, X., Zhang, J., Ding, M., Guo, Y., & Su, J. 2011, ApJ, 732, 87
Démoulin, P., & Aulanier, G. 2010, ApJ, 718, 1388
Fan, Y., & Gibson, S. E. 2007, ApJ, 668, 1232
Harrison, R. 2003, AdSpR, 32, 2425
Kliem, B., Lin, J., Forbes, T. G., Priest, E. R., & Török, T. 2014, ApJ, 789, 46
Kliem, B., Su, Y. N., van Ballegooijen, A. A., & DeLuca, E. E. 2013, ApJ, 779, 129
Kliem, B., & Török, T. 2006, PhRvL, 96, 255002
Lemen, J. R., Akin, D. J., Boerner, P. F., et al. 2011, The Solar Dynamics Observatory (Berlin: Springer), 17
Liu, C., Deng, N., Liu, R., et al. 2015, ApJL, 812, L19
Liu, L., Wang, Y., Wang, J., et al. 2016a, ApJ, 826, 119
Liu, R., Chen, J., Wang, Y., & Liu, K. 2016b, NatSR, 6, 34021
Liu, R., Liu, C., Wang, S., Deng, N., & Wang, H. 2010, ApJL, 725, L84
Liu, R., Kliem, B., Titov, V. S., et al. 2016, ApJ, 818, 148
Liu, Y. 2008, ApJL, 679, L151
Myers, C. E., Yamada, M., Ji, H., et al. 2015, Natur, 528, 526
Myers, C. E., Yamada, M., Ji, H., et al. 2016, PhPl, 23, 112102
Myers, C. E., Yamada, M., Ji, H., et al. 2017, PPCF, 59, 014048
Pesnell, W. D., Thompson, B. J., & Chamberlin, P. C. 2012, SoPh, 275, 3
Priest, E., & Forbes, T. 2002, A&ARv, 10, 313
Scherrer, P. H., Schou, J., Bush, R., et al. 2012, SoPh, 275, 207
Shibata, K. 1998, Ap&SS, 264, 129
Sun, X., Bobra, M. G., Hoeksema, J. T., et al. 2015, ApJL, 804, L28
Titov, V., & Démoulin, P. 1999, A&A, 351, 707
Török, T., & Kliem, B. 2005, ApJL, 630, L97
Török, T., & Kliem, B. 2007, AN, 328, 743
van Tend, W., & Kuperus, M. 1978, SoPh, 59, 115
Wang, W., Liu, R., Wang, Y., et al. 2017, NatCo, submitted
Wang, Y., & Zhang, J. 2007, ApJ, 665, 1428
Xu, Y., Liu, C., Jing, J., & Wang, H. 2012, ApJ, 761, 52
Yashiro, S., Gopalswamy, N., Akiyama, S., Michalek, G., & Howard, R. A. 2005, JGRA, 110, A12S05
Zhang, J., Dere, K., Howard, R., Kundu, M., & White, S. 2001, ApJ, 559, 452
Zhang, J., Dere, K., Howard, R., & Vourlidas, A. 2004, ApJ, 604, 420
Zuccarello, F., Aulanier, G., & Gilchrist, S. 2016, ApJL, 821, L23
Zuccarello, F. P., Aulanier, G., & Gilchrist, S. A. 2015, ApJ, 814, 126
Zuccarello, F. P., Seaton, D. B., Mierla, M., et al. 2014, ApJ, 785, 88